Rock Mechanics and Rock Engineering
https://doi.org/10.1007/s00603-024-04052-9

ORIGINAL PAPER

Beyond the Surface: Non-Invasive Low-Field NMR Analysis of Microbially-Induced Calcium Carbonate Precipitation in Shale Fractures

Matthew R. Willett[1,2] · **Kayla Bedey**[2,3] · **Dustin Crandall**[4] · **Joseph D. Seymour**[1,2] · **Jonny Rutqvist**[5] · **Alfred B. Cunningham**[2,3] · **Adrienne J. Phillips**[2,3] · **Catherine M. Kirkland**[2,3]

Received: 28 January 2024 / Accepted: 23 June 2024

Abstract

Microbially-induced calcium carbonate precipitation (MICP) is a biological process in which microbially-produced urease enzymes convert urea and calcium into solid calcium carbonate ($CaCO_3$) deposits. MICP has been demonstrated to reduce permeability in shale fractures under elevated pressures, raising the possibility of applying this technology to enhance shale reservoir storage safety. For this and other applications to become a reality, non-invasive tools are needed to determine how effectively MICP seals shale fractures at subsurface temperatures. In this study, two different MICP strategies were tested on 2.54 cm diameter and 5.08 cm long shale cores with a single fracture at 60 ℃. Flow-through, pulsed-flow MICP-treatment was repeatedly applied to Marcellus shale fractures with and without sand ("proppant") until reaching approximately four orders of magnitude reduction in apparent permeability, while a single application of polymer-based "immersion" MICP-treatment was applied to an Eagle Ford shale fracture with proppant. Low-field nuclear magnetic resonance (LF-NMR) and X-Ray computed microtomography (micro-CT) techniques were used to assess the degree of biomineralization. With the flow-through approach, these tools revealed that while $CaCO_3$ precipitation occurred throughout the fracture, there was preferential precipitation around proppant. Without proppant, the same approach led to premature sealing at the inlet side of the core. In contrast, immersion MICP-treatment sealed off the fracture edges and showed less mineral precipitation overall. This study highlights the use of LF-NMR relaxometry in characterizing fracture sealing and can help guide NMR logging tools in subsurface remediation efforts.

Extended author information available on the last page of the article

Highlights

- Engineered biological mineral precipitation can seal shale fractures at high temperatures.
- Nuclear magnetic resonance measures signal from hydrogen (water) and can characterize the extent of sealing inside rock fractures.
- Repeated delivery of aqueous precipitation solutions fills fractures thoroughly but is time-consuming and affected by distribution of sand grains inside the fracture.
- A single application of polymer-based precipitation solution seals fractures quickly but faces practical challenges.

Keywords MICP · Shale · NMR · Micro-CT · Carbon sequestration

1 Introduction

1.1 Background

Shale is a fine-grained, sedimentary rock often found adjacent to layers of sandstone and limestone up to thousands of feet below ground surface (bgs). The unique characteristics of this formation have led it to play multiple roles in the ever-changing energy landscape of the twenty-first century. Possessing lower porosity and permeability compared to conventional rock reservoirs, shale has been targeted for geologic nuclear waste disposal (Hansen et al. 2010), carbon sequestration (Rutqvist 2012; Espinoza and Santamarina 2017) and underground storage of hydrocarbons (Jeanne et al. 2020) and hydrogen (Zivar et al. 2021). Many shale deposits also contain rich quantities of hydrocarbon fuels, which can be extracted from very tight pore spaces with hydraulic fracturing (Soeder 2018). All of these applications highlight the need for methods to control permeability to ensure long-term safety and utility of these reservoirs. For example, there may be a need for a method to seal fractures that arise in shale used for storage purposes to mitigate leakage. There is also motivation to plug fractures created in hydraulic fracturing wells to prevent contamination of aquifers or to potentially restimulate the well to enhance natural gas recovery (Barba et al. 2022). Additionally, in geothermal systems within fractured crystalline rock, sealing the widest short-circuit fractures can improve zonal isolation for more efficient geothermal energy production (Petty et al. 2013; Cladouhos et al. 2016).

One promising solution is to induce calcium carbonate ($CaCO_3$) mineralization within shale fractures to seal possible fluid pathways using a process known as microbially-induced calcium carbonate precipitation (MICP). This “biocementation” technology was first used in the early 1990s to consolidate and plug sand columns (De Muynck et al. 2010). Since then, studies show that MICP-treatment can strengthen soil and seal cracks in stone and concrete structures (Phillips et al. 2013). The success of MICP can be attributed to the fact that it is delivered with non-toxic, low viscosity (aqueous) fluids and microbes that can permeate through small apertures. Indeed, its practicality has led to several successful applications in the field, including sealing sandstone fractures and remediating cement wellbores up to thousands of feet bgs (Cuthbert et al. 2013; Phillips et al. 2016, 2018; Kirkland et al. 2020, 2021). Applying this technology to seal shale fractures at depth, however, presents a new challenge to its viability due to severe subsurface conditions, where temperatures can range from 50 to 90 °C and pressures reach over 30 MPa (Hasan and Reza 2019).

1.2 MICP

MICP occurs through the degradation of urea, one of the mechanisms involved in the nitrogen cycle (Jain et al. 2021). In the first step, microbially-produced urease enzymes catalyze the hydrolysis of urea into carbamic acid and ammonia (Eq. 1). Additional hydrolysis reactions convert carbamic acid to carbonic acid and ammonia to ammonium and hydroxide (Eqs. 2–3). These ions increase the pH of the environment and lead to the formation of bicarbonate and then carbonate (Eqs. 4–5). Finally, in the presence of calcium, solid calcium carbonate biomineral is formed (Eq. 6) (Phillips et al. 2013):

$$CO\left(NH_2\right)_2 + H_2O \xrightarrow{urease} NH_2COOH + NH_3 \tag{1}$$

$$NH_2COOH + H_2O \rightarrow NH_3 + H_2CO_3 \tag{2}$$

$$2NH_3 + 2H_2O \leftrightarrow 2NH_4^+ + 2OH^- \tag{3}$$

$$H_2CO_3 \leftrightarrow HCO_3^- + H^+ \tag{4}$$

$$HCO_3^- + H^+ + 2OH^- \leftrightarrow CO_3^{2-} + 2H_2O \tag{5}$$

$$Ca^{2+} + CO_3^{2-} \leftrightarrow CaCO_3(s) \tag{6}$$

Many bacterial strains produce urease, but *Sporosarcina pasteurii* has been favored for MICP engineering applications due to its high ureolytic activity and biomineral formation rate (Jain et al. 2021). Successful precipitation of $CaCO_3$ is governed by four parameters: (1) dissolved inorganic carbon concentration (*i.e.* urea concentration), (2) pH of the environment, (3) calcium concentration, and (4) presence of nucleation sites for mineral formation (Phillips et al. 2013). The fourth condition presents perhaps the greatest challenge for shale biomineralization under subsurface conditions. While $CaCO_3$ nucleation is complex and may be influenced by many factors, it is generally assumed that microbes themselves serve as nucleation sites for precipitation (Wang 2018). If this is the case, cell attachment within shale fractures is critical for effective sealing. However, elevated temperatures and the complex nature of shale surfaces will significantly impact this process. Studies show that peak ureolytic activity for *S. pasteurii* is up to 70 ℃ (Whiffin 2004; Kim et al. 2018). However, at 60 ℃, ureolytic microorganisms are inactivated quickly (Hommel et al. 2020) and urease activity is reduced by 90% after 24 h (Bachmeier et al. 2002; Wang et al. 2023). Optimal temperatures for calcite precipitation are even lower, ranging from 30 to 50 ℃ (Kim et al. 2018). Meanwhile, shale lithology is highly intricate, containing a wide range of silicates, carbonates, clays, and organic matter (Livo et al. 2020). Only one study has reported the effectiveness of MICP on such complex surfaces. Cunningham et al. (2015) demonstrated that clay-rich, Opalinus shale cores with a single fracture filled with 30/50 sand ("proppant") could be biomineralized under ambient conditions, achieving up to four orders of magnitude permeability reduction after four days of repeat MICP injections. Significantly, one order of magnitude permeability reduction was reached when biomineralizing under high-pressure conditions of 6.12 MPa (Cunningham et al. 2015). While this demonstrates that MICP-treatment of shale may be feasible, further research is needed to explore treatment at elevated temperatures, more efficient MICP delivery strategies, and develop non-invasive tools to determine sealing efficacy.

1.3 Polymer-Modified MICP

Several recent studies suggest that polymer additives have potential to speed up and even enhance MICP-treatment of porous media. In MICP-treated packs of martian and lunar regolith, the addition of 1% m/v guar to MICP solutions improved the mechanical strength of the consolidated rock by up to sixfold (Dikshit et al. 2021, 2022). Guar (0.7% m/v) has also been successfully used in enzymatically induced calcium carbonate composite adhesives (Anjum 2023). In another study, polyvinyl alcohol (PVA) polymer played a critical role in the success of a "one-shot" MICP-treatment strategy of Ottawa sand packs (Wang and Tao 2018). The enhanced viscosity of the MICP solutions improved delivery to high permeability regions and lead to uniform $CaCO_3$ precipitation. Since guar is a widely used additive in hydraulic fracturing (Meng et al. 2021), it will be explored in this study to test a single-shot, polymer-based sealing approach termed "immersion" MICP for comparison to the flow-through, water-based MICP approach.

1.4 NMR

One non-invasive approach to study the effectiveness of shale biomineralization is nuclear magnetic resonance (NMR). A sample placed in an NMR magnet is exposed to a static $\mathbf{B_0}$ magnetic field which causes ^{1}H nuclei (*i.e.* protons) within the sample to align their magnetic moments together and form a net magnetization $\mathbf{M_0}$ (Callaghan 1991; Blümich 2005). In a process called "excitation", $\mathbf{M_0}$ is manipulated by radiofrequency (RF) pulses to create signal. NMR is highly sensitive to water and signal amplitude is proportional to the total amount of protons present. Moreover, in porous media saturated with water, the rate of signal decay, termed T_2 relaxation, is proportional to the pore surface-to-volume ratio (S/V) in $[1/m]$ (Eq. 7):

$$\frac{1}{T_2} = \frac{1}{T_{2B}} + \rho_2 \frac{S}{V} \tag{7}$$

where T_2 is the overall T_2 relaxation time of the pore in $[s]$, T_{2B} is the intrinsic T_2 relaxation time of the "bulk" pore fluid in $[s]$, and ρ_2 is the surface relaxivity for T_2 relaxation in $[m/s]$ (Callaghan 2011). Surface relaxivity describes the rate of magnetization decay induced by the pore wall and is influenced by the rock lithology, particularly paramagnetic compounds (Brownstein and Tarr 1979; Kleinberg et al. 1994; Cheng et al. 2023). When S/V is large, as in the case of shale nanopores, T_2 relaxation will be dominated by interactions between protons and surfaces and the influence of T_{2B} will be negligible. Conversely, if S/V is small, T_2 relaxation will be dominated by interactions between the protons themselves and have more bulk fluid relaxation behavior, *i.e.* longer T_2 relaxation times. Equation (7) is also valid at describing T_2 relaxation within fractures (Golsanami et al. 2016). The difference between the S/V of large fractures ($>>0.2$ mm gap) and shale nanopores makes it possible to distinguish the relaxation times of these two hydrogen populations. Equation (7) establishes that an NMR T_2 experiment, which measures the distribution of T_2 relaxation times within a sample, can also be used to characterize the distribution of pore sizes and fractures within a porous media.

While NMR relaxometry forms the basis of NMR logging tools widely used to characterize porosity and permeability in oil and gas wells (Kirkland and Codd 2018), NMR signal from shale is complicated because significant amounts of hydrogen can also exist in organic material such as kerogen and bitumen (Washburn 2014). Fortunately, signal from the various ^{1}H components can be distinguished by exploiting differences in NMR T_1 relaxation times. T_1 relaxation is distinct from T_2 relaxation and describes how protons return to thermal equilibrium following excitation (Gupta et al. 2021). Motionally restricted components, which include most of the organics in shale, have $T_1/T_2>1$, while water displays $T_1/T_2 \approx 1$ (Fleury and Romero-Sarmiento 2016). NMR T_1-T_2 relaxation correlation experiments provide another dimension to separate signal and characterize the various hydrogen populations.

Overall, NMR is well-equipped to analyze shale fractures undergoing biomineralization. Tracking how the organic hydrogen, pore water, and fracture water populations change after MICP-treatment can reveal the extent of biomineralization. To the author's knowledge, there are no prior studies using NMR to analyze biomineralized shale fractures. However, Jin et al. (2020) used NMR relaxometry to study freeze–thaw cycles on shale soils consolidated with MICP-treatment. Increases in T_2 relaxation times and signal were observed in many pores, indicating they were damaged and enlarged by freeze–thaw cycles. Many studies have also used NMR to characterize MICP-treated sandstone. Sandstone is generally more porous and has much greater permeability than shale (Washburn 2014). As expected, NMR revealed that MICP occurs throughout the pore network (Sham et al. 2013; Zhuang et al. 2022). Also relevant are NMR studies of biomineralized sand columns. In shale, fractures can be filled with proppant and microbes are expected to attach to the sand particles as well as the shale. Interestingly, two studies reported that in sand columns undergoing MICP-treatment, water in large pores had longer T_2 relaxation times post-MICP despite an overall reduction in signal (Kirkland et al. 2017; Thrane et al. 2020). In these systems, mineral formation and/or gas bubbles generated during precipitation shielded water from paramagnetic impurities of the sand, effectively reducing ρ_2 and causing an increase in T_2 relaxation times. However, another study by Wu et al. (2017) reported the opposite trend: enhanced T_2 relaxation along with lower signal from macropore peaks as sand columns were progressively biomineralized. In this system, $CaCO_3$ filled voids around sand, lowering S/V and causing a reduction in T_2 relaxation times. These findings demonstrate that MICP-treatment of porous media can produce complex NMR results. It is not always apparent whether changes in S/V or ρ_2 will have a greater impact on NMR relaxation. However, while relaxation times of water in large shale fractures are expected to be similar to those of bulk water, it is likely shale surfaces will enhance T_2. In this case, mineral precipitation on the fracture surfaces may cause T_2 to initially increase before changes in S/V has an impact.

1.5 X-Ray Computed Microtomography (micro-CT)

Despite the versatility of NMR, its characterization of shale is largely limited to bulk measurements. While NMR imaging, also known as magnetic resonance imaging (MRI), can spatially localize signal, this is difficult with shale since NMR signal decays rapidly and pushes the limits of conventional signal detection and acquisition (Zamiri et al. 2022). Instead, X-Ray computed microtomography (micro-CT) scanning, another non-invasive tool, can be used obtain spatially resolved information. Micro-CT scanners work by taking multiple X-Ray measurements at different angles around a sample (Jung 2021). X-Rays are absorbed or scattered to varying degrees depending on the type of materials they encounter and then transmitted to a detector. Two-dimensional (2-D) cross-sectional images are reconstructed from a series of one-dimensional (1-D) X-Ray projections. Fortunately, characterizing micro-CT signal is much more straightforward than NMR: dark areas in a micro-CT image represent empty spaces and bright regions represent solid materials. Micro-CT can provide a visual of mineral deposition within the fracture as well as quantifiable, spatial measurements of changes in the void fraction due to MICP. Using micro-CT to characterize biomineralization in porous media has been well established (Minto et al. 2017; Tobler et al. 2018; Kirkland et al. 2019; Sang et al. 2022; Turner et al. 2023).

In this study, LF-NMR methods are developed and applied to characterize the extent of biomineralization in shale fractures. Core specimens undergo flow-through MICP-treatment with and without proppant at 60 °C, a temperature reflective of subsurface conditions in shallow shale plays (Hasan and Reza 2019). Micro-CT is used to corroborate NMR findings. Comparisons are made between the complimentary information provided by each approach as well as a discussion on their unique insights. Lastly, these non-invasive methods are used to assess a faster, single-shot sealing strategy which utilizes polymer-modified MICP solutions. Ultimately, determining the effectiveness of MICP-treatment at the lab scale is a critical step before deployment in the subsurface.

2 Materials and Methods

2.1 Materials

Flow-through MICP-treatment was conducted on Marcellus shale reservoir samples provided by the National Energy Technology Laboratory (NETL) and sourced from the Yawkey No. 98 vertical well in Logan County, West Virginia at a depth of 4000–4171.6 ft. Cores 2.54 cm (1 in.) in diameter were drilled perpendicular to the bedding plane and cut into 5.08 cm (2 in.) lengths. A full description of the Yawkey shale can be found in Crandall et al. (2019). Immersion MICP-treatment was conducted on outcrop Eagle Ford shale from Texas (Kocurek Industries, Caldwell, TX) which were drilled parallel to the bedding plane with the same dimensions as the Marcellus samples.

All cores were split in half lengthwise using a modified Brazilian test method. To prepare for preliminary NMR and micro-CT measurements, the fracture surfaces were cleaned and one layer of Granusil 2095 size (10/20) sand was spread evenly along one half of the fractured shale. Next, the other half was placed on top, and both pieces were wrapped together with Teflon tape. The sample without proppant was created by affixing four square pieces of 3.5 × 3.5 mm Teflon PTFE (0.5 mm thick, McMaster-Carr) to each corner of one of the fracture halves with epoxy before securing both halves together with Teflon tape.

2.2 X-Ray Diffraction (XRD) Analysis

XRD was utilized to determine shale mineralogical composition. Representative shale samples were ground lightly in a mortar and pestle, sieved to < 60 µm, and scanned by a Bruker D8 Advance Powder X-Ray Diffractometer at the Imaging and Chemical Analysis Laboratory (ICAL) at Montana State University (MSU). The spectra were obtained using the Cu K-alpha line at 1600 W. The mineral composition was identified by peak fitting using JADE analysis software (ICDD) using search match with the PDF-4 + standards database, with a detection limit of approximately 1–5%. Quantitative analysis was performed using the Rietveld peak-fitting algorithm for identified phases.

2.3 NMR Measurements

Instrumentation consisted of a low-field, benchtop 2 MHZ Magritek Rock Core Analyzer (RCA) with a 54 mm probe (Magritek, Wellington, New Zealand). Low-field NMR (LF-NMR) exposes the sample to weaker $\mathbf{B_0}$ magnetic fields compared to high-field instruments, which reduces the impact of magnetic field susceptibility artifacts. LF-NMR also forms the basis for NMR logging tools (Kirkland and Codd 2018).

To prepare the sample for NMR analysis, shale cores were saturated in brine for 24–48 h under vacuum (Thermo Scientific Nalgene Vacuum Chamber). Subsequently, they were quickly wrapped in Teflon tape, filled with brine to occupy the fracture, and sealed with an additional Teflon tape cover. T_2 experiments were measured by the Carr-Purcell-Meiboom-Gill (CPMG) pulse sequence. Multi-exponential signal was inverted by the inverse Laplace method to generate a T_2 distribution. T_1-T_2 correlation experiments consisted of an initial inversion recovery sequence followed by a CPMG train. Signal was inverted with the 2-D inverse Laplace method to generate a T_1 versus T_2 distribution. The inverse Laplace transform was calculated using a non-negative least square (NNLS) fitting function and Tikhonov regularization to minimize the error (Venkataramanan et al. 2002; Callaghan et al. 2003). Experiment parameters are shown in Table 1.

2.4 Micro-CT Scanning

Prior to micro-CT analysis, shale cores were thoroughly dried for 24–48 h at 60 ℃ and then fully wrapped in Teflon. Instrumentation consisted of a Skyscan 1173 X-Ray microtomograph (Bruker Corporation, MSU Subzero Science Laboratory). Image resolution was 17.3 µm. To create a complete image of the core, three overlapping sections were scanned every 0.7° for 180°. An exposure of 1200 ms, a voltage of 130 kV, and a current of 60 µA with a brass 0.25 mm filtered beam were used to capture all scans. Prior to each scan a flat field correction was performed to calibrate the initial intensity of the beam. The three overlapping sections of the scans were reconstructed using NRecon software (Bruker Corporation) to produce a series of 2-D images, or slices, representing the length of the core. Gaussian kernel smoothing was used during reconstruction to remove noise. Once reconstructed, a circular region of interest (ROI) was drawn around the circumference of the core for each 2-D slice using CTAn software (Bruker Corporation).

Slices were made binary in CTAn by applying Bruker's global thresholding algorithm to distinguish shale, proppant, and mineral from void space. The data was sorted into two tonalities, with black pixels representing void space within the fracture and white pixels representing shale, proppant, and mineral, which show similar attenuation. The ideal thresholding range was determined by maintaining the maximum grayscale value for an 8-bit image and manually adjusting the minimum value in the histogram of grayscale values to best represent the void space inside the fracture based on the reconstructed grayscale slices. CTAn was used to calculate the area of black pixels in each slice of the scan

Table 1 NMR experimental parameters

Parameter	T_2	T_1-T_2
Repetition time (s)	10	10
Echo time (µs)	100–400	100
Number of echoes (1000 s)	7.5–50	30–40
Number of scans	8–128	128
Number of T_1 delays	n/a	32
Min–Max T_1 delay (ms)	n/a	0.1–10,000

to estimate the fracture pore volume. Aperture map profiles were created in Fiji from the extracted fracture volumes (Schindelin et al. 2012).

To account for potential variability in the threshold selection, the threshold value was adjusted by ± 8 grayscale values, which corresponds to a small fraction of the dynamic range of an 8-bit image. The images were segmented using these adjusted threshold values and the corresponding pore volumes calculated. The range of these volumes (from the minimum to the maximum) provides an estimate of the uncertainty introduced by the thresholding process.

2.5 Media

100 mL of brain heart infusion (37 g/L) amended with urea (20 g/L) was inoculated with 1 mL thawed frozen stock culture of *S. pasteurii* (ATCC 11859). After 24 h., the culture was transferred into yeast extract (YE) media (1% v/v). YE media consisted of 1 g/L ammonium chloride, 15.5 g/L yeast extract, 35 g/L sodium chloride, and 20 g/L urea. After 16 h., the bacteria concentration was assessed by injecting 200 µL of culture into a Greiner Bio-One 96 well flat bottom plate and measuring the optical density (OD) with a Tecan Infinite F50 absorbance reader with a 600 nm filter. OD_{600} readings > 0.6 were considered high bacteria concentrations and used for injections. Calcium mineralizing media (CMM) was prepared by combining 20 g/L of urea, 35 g/L sodium chloride, 1 g/L ammonium chloride, and 3 g/L nutrient broth; adjusting pH to 6–6.3 with 0.1 M HCl; and then adding 48 g/L calcium chloride dihydrate. CMM solution prepared without nutrient broth was labeled "U + C" (urea and calcium). Brine consisted of 35 g/L sodium chloride.

2.6 Apparent Permeability

Flow through a shale fracture can be estimated as flow through a porous media with high permeability. Under laminar flow and low Reynolds numbers, Darcy's Law can describe flow through a porous medium: (Eq. 8):

$$k = \frac{Q \bullet \Delta L \bullet \mu}{A \bullet \Delta P} \tag{8}$$

where k is the hydraulic permeability, Q is the volumetric flow rate of the fluid, μ is the viscosity of the fluid, A is the cross-sectional area of the flow path, ΔL is the length of the core/fracture, and ΔP is the pressure drop across the flow path (Zimmerman and Bodvarsson 1996). As the fracture aperture is constantly changing, calculating k presents certain challenges. Instead, $Q/\Delta P$, or the "apparent permeability", will be reported in $[cm^3/Pa \bullet s]$, which represents the resistance to flow and is useful to gauge the progress of biomineralization within the fracture.

2.7 Flow-Through MICP Experimental Design

2.7.1 Flow-Through Reactor System

The reactor system consisted of two piston ISCO syringe pumps which separately delivered microbes or U + C to the core holder inside a 60 ℃ oven (Fig. 1). The pump delivering U + C was also equipped with a heated water jacket maintained at 60 ℃. Pressure was recorded from an Omega Engineering, Inc. PX309 series pressure transducer and Campbell manual pressure gauge. The various components were connected by 1/4-in. OD stainless steel tubing.

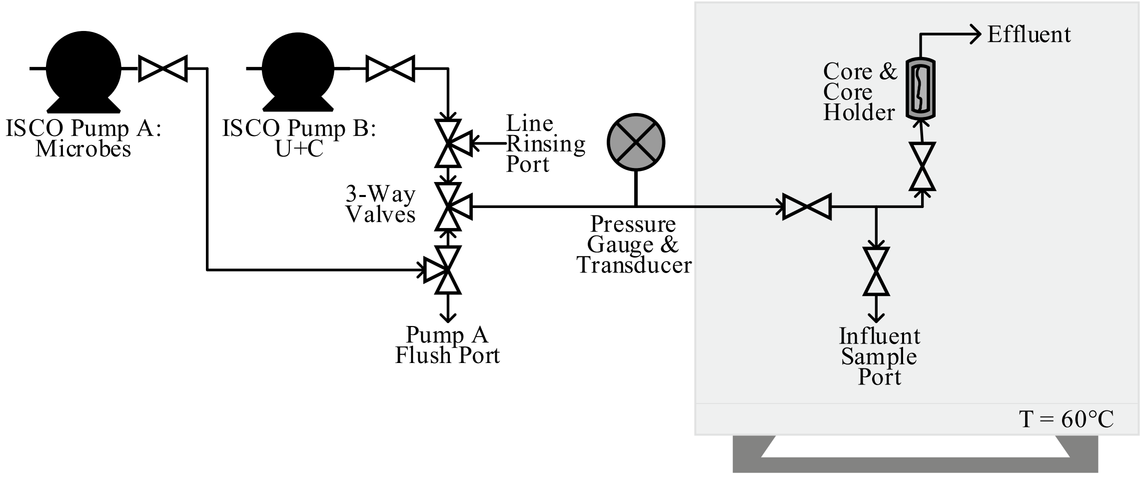

Fig. 1 Schematic of the reactor system. Pump A delivered *S. pasteurii* culture to the core inside a 60 ℃ oven. Following a brief attachment period, pump B delivered pre-heated urea and calcium (U + C) media also at 60 ℃ to the core. This was followed by a resting 2 h. batch period. Pressure drop across the core was measured with a pressure transducer or gauge in order to calculate the apparent permeability for each injection

The core holder consisted of a 15.24 cm length of 2.54 cm diameter reinforced clear PVC tubing (McMaster-Carr). The Teflon-wrapped core was enclosed in FEP heat shrink tubing (McMaster-Carr) and then inserted into the PVC tubing. Additional overburden pressure was provided by two heavy duty hose clamps placed around both ends of the core, which were tightened to 3.4–4.5 N-m with a torque-wrench. The core holder was connected to the stainless steel tubing system with a hose adapter fitting and rubber tubing. The maximum pressure of the core holder was estimated to be 207 kPa.

2.7.2 Flow-Through Injection Strategy

A pulsed-flow, staged injection strategy was employed in this study. First, the core was inoculated with *S. pasteurii* culture and allowed to rest for 15 min, a relatively brief "attachment period" to limit inactivation of cells and urease through exposure to elevated temperatures. Next, U + C was pulsed at 5 mL/min until reaching the core inlet, then 1 mL/min while flowing through the core. After delivering 1–2 times the fracture volume, the valve beneath the core was closed and the reaction was allowed to proceed for a two-hour period. Resting batch periods were concluded with a brine flush. Flow rates of all media were adjusted/lowered with each subsequent injection to ensure pressure did not exceed system limits. MICP pulsed-flow treatments were continued until reaching at least 3 orders of magnitude apparent permeability reduction.

2.8 Immersion MICP Experimental Design

The polymer-based solution for immersion MICP was prepared by first making CMM as outlined in Sect. 2.5 but doubling the concentration of urea and calcium (2 × CMM). Guar gum (Carolina Biological Supply) was added until reaching a concentration of 1.5% m/v. Meanwhile, 200 mL of *S. pasteurii* culture was spun down at 2964×*g* for 10 min at 4 ℃ (Thermo Scientific Sorvall Legend XTR Centrifuge) and the supernatant removed. The cells were resuspended in 50 mL of the 2 × CMM and guar solution ($OD_{600} > 1.8$). After thoroughly mixing, approximately 3 mL of this "slug" was directly applied to one half of a shale fracture with a single layer of Granusil 2095 size (10/20) sand. After placing the other half on top, the center of the core was wrapped in 1/2-in. Teflon tape and the composite core was placed in a 60 °C oven for a 30-min attachment period. Next, the core was immersed in U + C solution and placed in the same 60 °C oven for a 4-h reaction period. Finally, the core was removed from the solution and incubated for five days at 40 ℃.

2.9 Experimental Workflow

Figure 2 illustrates an overview of the measurements and experiments for this study. Two different biomineralization techniques will be explored, resulting in three sealed shale fractures: flow-through MICP-treatment with and without proppant and immersion MICP-treatment with proppant, all conducted at 60 ℃.

3 Results and Discussion

3.1 Mineralogical Composition of Marcellus and Eagle Ford Shale

The Marcellus shale samples sourced from the Yawkey well and used in flow-through MICP-treatment contained roughly equal amounts of quartz (48%) and clays (muscovitie/illite and chlorite) (49%). No carbonates (calcite or dolomite) were detected. Note that this sample was specifically from

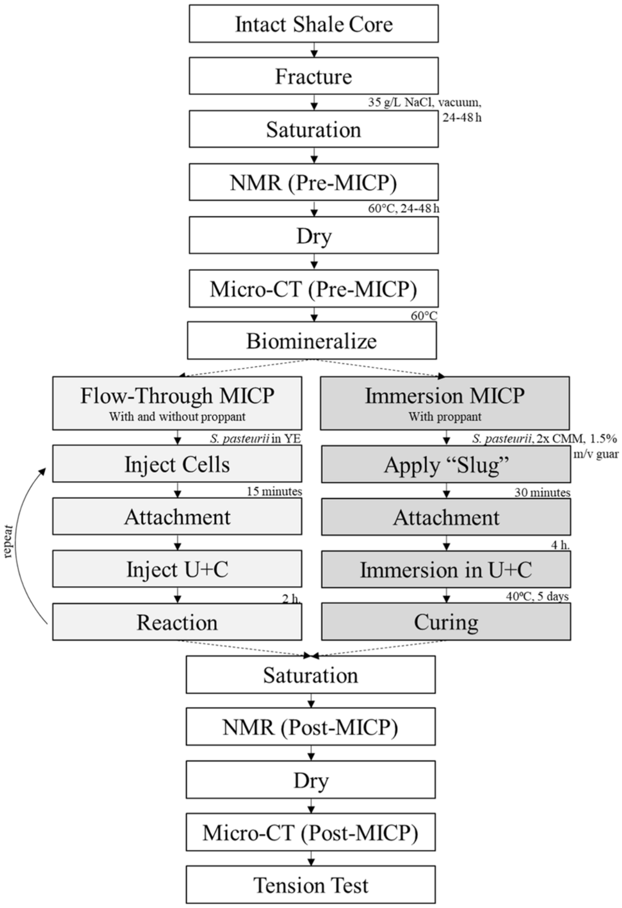

Fig. 2 Schematic of the experimental workflow. Following the non-invasive testing, mechanical properties of the biomineralized shale core will be analyzed with tensile strength testing (Bedey et al. 2023)

the core used in flow-through MICP-treatment with proppant; a representative sample was not available for the core without proppant. The outcrop Eagle Ford shale samples used in immersion MICP-treatment contained a majority carbonate content (75% calcite and 2% dolomite), with some quartz (21%) and an undetectable amount of clays. Table 2 shows the complete mineralogical breakdown of the shale samples as detected by XRD.

3.2 Characterizing NMR Signal from Fractured Shale

Before analyzing NMR results from the biomineralized cores, it was important to confirm that signal from a single, large fracture was distinguishable from the various shale hydrogen populations. Figure 3 shows the T_1-T_2 relaxation correlations for a saturated Marcellus shale core, pre- and post-fracture. The intact core (top) displays dominant signal along the line $10 < T_1/T_2 < 1000$ at T_2 ~0.1 ms, a regime attributed to bitumen, kerogen, and structural water within the shale (Mukhametdinova et al. 2021). However, due to the echo time limitation, NMR signal thatdecays before 0.1 ms cannot be fully resolved. Spectral features generated by the inverse Laplace transform before this value are questionable. Shorter echo times or alternative pulse sequences such as the T_1-T_2^* measurement may be able to completely characterize these populations, but the focus of this study will be analyzing water within shale fractures pre- and post-MICP with spin-echo experiments (Zamiri et al. 2021). To that end, signal from water within the shale appears along the parity line T_1/T_2 ~1 and $0.1 < T_2 < 10$ ms, the motionally narrowed liquid regime. Since clay-bound water signal appears around the limit of detection, this signal can be mostly attributed to water trapped within the shale "micropores" (< 100 nm) and "mesopores" (100–1000 nm) (Zhang et al. 2020). Certainly, what is missing from the T_1-T_2 relaxation correlation is equally important as what it reveals. There is no signal from larger shale pores, *i.e.* "macropores" (> 1000 nm), which has a reported signature along the parity line between $10 < T_2 < 1000$ ms (Mukhametdinova et al. 2021). Moreover, free or adsorbed oil, a potentially major organic component expected to appear at $T_1/T_2 > 10$ and $0.1 < T_2 < 100$ ms, is also absent (Mukhametdinova et al. 2021). This is not unusual as shale rock can have a wide degree of variability. This particular sample appears to possess very tight pore spaces and comes from a well that is not oil-rich.

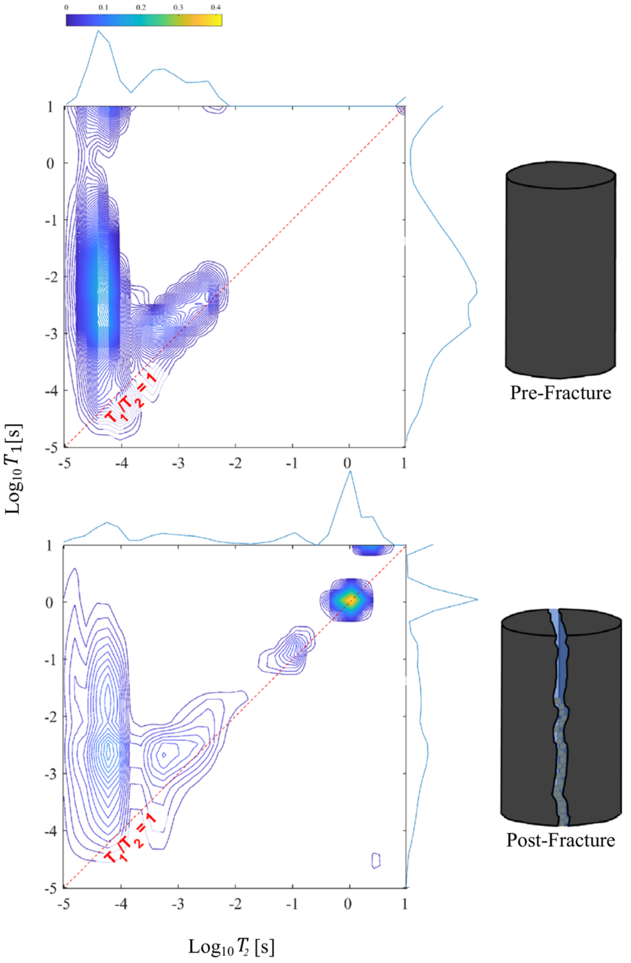

Fig. 3 T_1-T_2 map of a saturated Marcellus shale core before (top) and after (bottom) creating a fluidized fracture with sand "proppant." T_1-T_2 correlations can separate the contributions from the different shale hydrogen populations

The fractured shale core contains ~ 1 mm sand grains keeping the gap open. Water is held inside the fracture while NMR experiments are conducted. As expected, new signal from bulk water appears along $1 < T_1/T_2 < 10$ and $10 < T_2 < 10{,}000$ ms in the post-fracture T_1-T_2 correlation map (Fig. 3, bottom). This region contains multiple modes along the parity line at $T_2 = 116$ and 1067 ms, which reflects that this environment is a porous media in its own right. Multiple

Table 2 XRD analysis of shale samples undergoing MICP-treatment (ND: not detected)

Type	Location	Quartz (%)	Muscovite/illite (%)	Calcite (%)	Dolomite (%)	Pyrite (%)	Kaolinite (%)	Chlorite (%)
Marcellus	Logan Country, WV	48	47	ND	ND	2	ND	2
Eagle Ford	Caldwell, TX	21	ND	75	2	ND	2	ND

water populations are created by sand particles trapped between each other and the layers of shale. This raises a question of whether T_2 distributions of water within the fracture may overlap with the T_2 distributions of shale pore water. The previously identified shale micropore/mesopore range T_1/T_2 ~1 and $0.1 < T_2 < 10$ ms appears to extend to 20 ms post-fracture, however the integrated signal intensities are virtually unchanged pre-and post-fracture (< 2% drop). This indicates that it is unlikely that signal from the fracture overlaps with signal from the pores. The increase in the range of T_2 times may be a consequence of the 2-D ILT finding a slightly different fit due to the large increase in signal post-fracture (+67%). Signal beyond $T_2 > 10$ ms can therefore be designated as "fracture water." It is noteworthy that the most intense signal appears at the $T_2 = 1067$ ms mode, which is 17% lower than the T_2 time of pure brine (1292 ms). Most of the bulk water in the fracture behaves like 'free' water, with enhanced relaxation caused by paramagnetic impurities from surfaces. Since T_1-T_2 distributions of all biomineralized cores revealed no shale hydrogen populations overlapping with "fracture water" signal, T_2 distributions were exclusively used to characterize biomineralization (T_1-T_2 distributions are shown in Appendix A).

3.3 Analysis of Flow-Through Biomineralized Shale Core with Proppant

3.3.1 Apparent Permeability

The initial apparent permeability was calculated to be 1.7×10^{-3} cm^3/Pa•s at a flow rate of 5 mL/min through the fracture (Fig. 4). After 26 pulsed-flow injections, the apparent permeability was reduced by approximately four orders of magnitude to 3.3×10^{-7} cm^3/Pa•s at a flow rate of 0.03 mL/min, and the core was removed for NMR and micro-CT analysis. A comprehensive list of the pressures and flow rates used during each injection can be found in Appendix B. Photographs of both ends of the cores post-MICP revealed more extensive sealing at the effluent side versus the influent side, indicating precipitation was not uniform (Fig. 5).

3.3.2 NMR Analysis

Figure 6 shows the normalized T_2 profiles of the saturated Yawkey shale core, pre- and post-MICP. Both contain three modes labeled A, B and C from left to right. In the pre-MICP sample, modes B and C are found at 99.6 and 625 ms, respectively, and both possess strong intensities. This implies there are two main populations of bulk water within the fracture. During sample preparation, an even layer of proppant was spread along the length of the core, but after wrapping and setting the core upright for analysis, it was observed that sand particles not tightly pressed between both sides of the core moved down and accumulated at the bottom of the sample. This may have bifurcated the bulk water population into two main groups: restricted water in pore spaces created by proppant at the bottom, represented by peak B, and 'free' water at the top, represented by peak C. The latter has a T_2 time 52% lower than the T_2 time of pure brine, indicating significant surface relaxation despite the large fracture gap. Proton exchange, another relaxation mechanism, may also be acting to average the relaxation times between the different environments. Peak A is connected to Peak B and exists between the previously identified "pore water" and "fracture water" regions, though mostly the latter. This implies there could be overlap in signal between these two groups, however the gap in signal from $2 < T_2 < 5$ ms suggests that water from within this particular core is likely coming from micropores and structural/adsorbed water and that the "fracture water" T_2 distributions are distinct from these populations.

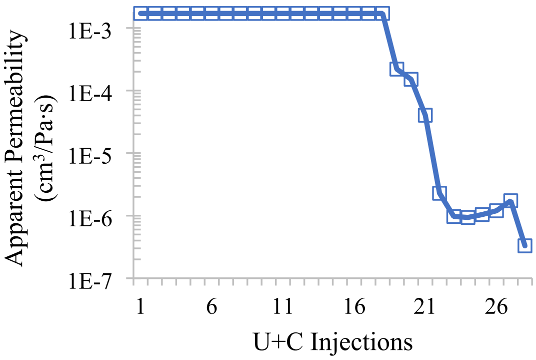

Fig. 4 Changes in apparent permeability over the course of MICP-treatment

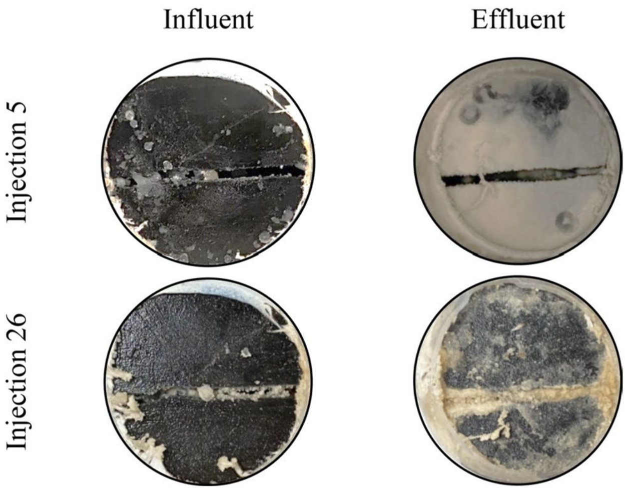

Fig. 5 Photographs of influent/effluent sides of the core after the 5th and 26th round of MICP-treatment

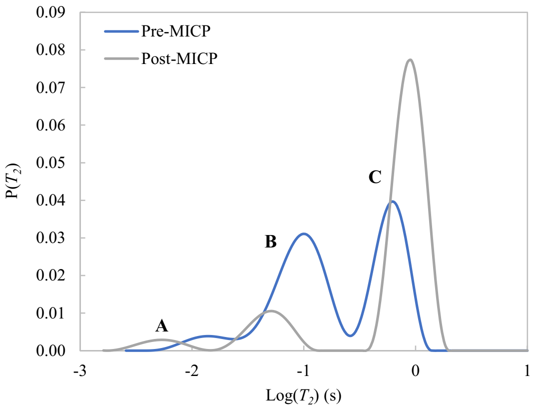

Fig. 6 Normalized T_2 distributions of a fractured, saturated Marcellus (Yawkey) shale core with proppant before (blue) and after (grey) MICP-treatment by the pulsed-flow, flow-through method. Peak C represents 'free' water inside the fracture and peaks A and B represent water bounded within pores created by proppant. Following biomineralization, all of the peaks reduced in intensity and moved to smaller T_2 relaxation times, except peak C. This suggests precipitation formed thoroughly around proppant but significant voids are still present inside the fracture. Additionally, the increase in the T_2 time of peak C implies a reduction in the surface relaxivity of the shale, caused by mineral preciptiation on surfaces

Post-MICP, peaks A and B shift to lower T_2 relaxation times (-60% and -48%, respectively) with lower intensity (-25% and -66%, respectively). Since these populations are closely associated with pore spaces created by proppant, the changes suggest that biomineralization is filling these voids. Calcium carbonate formation in a given pore space will displace water, resulting in less signal, and create a smaller pore size, resulting in enhanced T_2 relaxation. Peak C, on the other hand, shifts to a longer T_2 relaxation time and higher intensity (+47%, +95%, respectively) post-MICP. Since the total (accumulated) NMR signal lowers post-MICP (-35%), the increase in this population demonstrates that there is still a significant amount of empty space within the fracture for protons to behave as 'free' water. However, the increase in T_2 relaxation is indicative of a reduction in shale surface relaxivity, likely caused by calcium carbonate precipitation on shale surfaces.

Overall, the NMR data suggests biomineralization occurred throughout the fracture, though more thoroughly around regions associated with proppant. Proppant provides more surface area for microbes to attach and biomineral will likely first bridge both sides of the fracture at these locations. As a result, dense regions of proppant may seal off before precipitation has formed throughout the rest of the fracture. This phenomenon could explain why there is ample signal from 'free' water detected by NMR post-MICP while also observing a significant decrease in apparent permeability. Meanwhile, the increase in surface relaxivity reflects well on the ability of biomineral to precipitate on complex shale surfaces. However, as shale lithology is extremely diverse, this finding is limited to the specific mineralogical makeup of the sample used, *i.e.* clay- and quartz-rich shale (Table 2).

Table 3 T_2 modes from T_2 distributions in Fig. 6

Sample	T_2 Modes (ms)		
	A	B	C
Pre-MICP	13.1	99.6	625
Post-MICP	5.24	52.0	916

Unfortunately, hardware constraints obfuscate some potential insight provided by NMR. LF-NMR has lower signal compared to high-field NMR and it is difficult to resolve fast-decaying signal. These limitations make it impossible to track if precipitation is happening within the pores of the shale itself, as with sandstone (Sham et al. 2013; Zhuang et al. 2022). *S. pasteurii* cells have a length of 1.5–10 µm (Wang 2018) and are too large to diffuse through shale nanopores, though it is theoretically possible for calcium, urea and urease to do so. However, the highly permeable fracture undoubtedly presents a preferential flow path for these reactants, in contrast to the extremely low permeability of the shale. Biomineralization should dominate within the fracture and tracking water in this region is well within the capabilities of the NMR tools used in this study.

3.3.3 Micro-CT Analysis

Figure 7 displays how the void volume of the fracture quantified by micro-CT varies spatially along the direction of flow through the core, from 0 cm at the inlet side to 5 cm at the effluent side. In the pre-MICP data, there is significantly lower void volume (*i.e.* higher density) at the entrance of the core from approximately 0–0.6 cm. This is due to proppant accumulating at the inlet side after it was set upright for scanning. Proppant buildup at the entrance of the core can be seen in Fig. 8, the pre-MICP fracture aperture map. Nevertheless, many pieces are still firmly pressed between the shale halves further up along the core, especially around 4.5–5 cm near the effluent side.

The fracture aperture maps before and after MICP-treatment (Figs. 8 and 9, respectively) show that proppant shifted from the influent towards the effluent side of the fracture, resulting in a higher density of proppant at that end. Proppant was expected to redistribute during the experiment, from sample handling or hydrodynamic forces caused by injection of fluids. The migration of proppant, coupled with poor biomineral formation at the influent side, likely explains the higher void space (*i.e.* lower density) observed from 0 to 0.6 cm post-MICP compared to pre-MICP (Fig. 7).

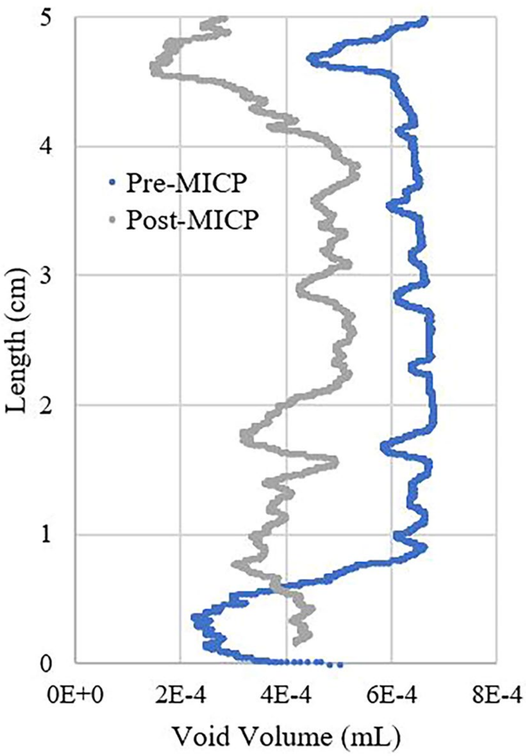

Fig. 7 Void volume calculated by micro-CT along the length of the fracture before (blue) and after (grey) MICP-treatment. Post-MICP, there is an overall decrease in the amount of void space present inside the fracture, though the greatest reduction occurs close to the effluent side around 4.6 cm

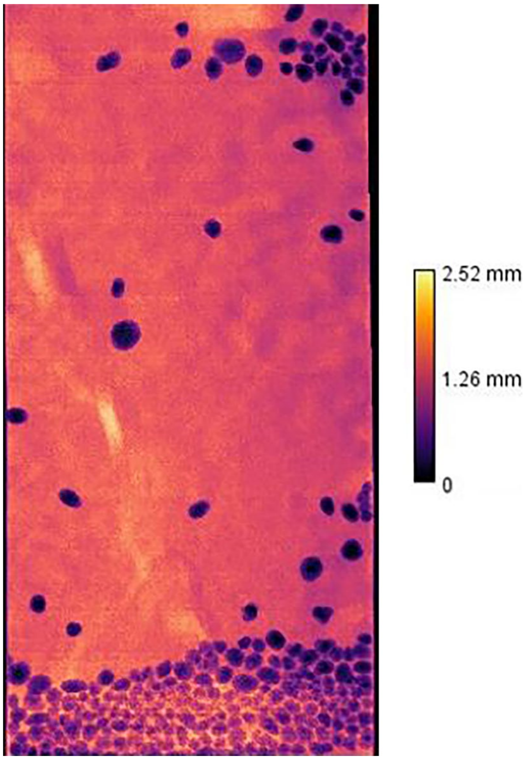

Fig. 8 Pre-MICP fracture aperture map generated from the micro-CT extracted fracture volumes. Proppant (30/50) accumulated at the bottom of the core during analysis, though other particles are still firmly pressed between both sides of the fracture in other locations

However, beyond this point, the void volume is noticeably lower along the length of the core, indicating biomineralization occurred throughout the fracture. Indeed, Fig. 9, the post-MICP fracture aperture map, reveals $CaCO_3$ precipitation along the surfaces inside the fracture. However, there is more buildup around dense areas of proppant, and it appears the core was plugged at the effluent side. It is notable that despite large voids regions still present through the fracture, the seal created near the effluent side was significant enough to achieve four orders of magnitude apparent permeability reduction and prevent further injections.

Preferentially plugging the effluent side of the core is unusual. Typically, the opposite trend is observed, given that the inlet side is exposed to reactants first (Phillips et al. 2013; Wang 2018). The goal of the pulsed-flow injection strategy is to avoid premature influent sealing by injecting reactants quickly and having the transport rate dominate over the reaction rate. Once reactants have reached the effluent side, flow is stopped, and the reaction rate is allowed to dominate and ideally lead to precipitation throughout the fracture. Ultimately, however, biomineral filled spaces around dense areas of proppant first, which happened to be at the effluent side of the core. Distribution of proppant within the fracture appears to be a significant factor controlling the degree of biomineralization.

3.4 Analysis of Flow-Through Biomineralized Core Without Proppant

3.4.1 Apparent Permeability

The initial apparent permeability (Fig. 10) of the shale fracture without proppant was 1.8×10^{-3} $cm^3/Pa{\bullet}s$ at a flow rate of 5 mL/min. Following 13 pulsed-flow injections, the apparent permeability reduced by approximately four orders of magnitude to 2.6×10^{-7} $cm^3/Pa{\bullet}s$ at a flow rate of 0.03 mL/min. A detailed list of the pressures and flow rates used during each injection can be found in Appendix B. Post-MICP visual inspection of both ends of the cores revealed that the inlet side of the fracture was plugged while the effluent side remained exposed (Fig. 11).

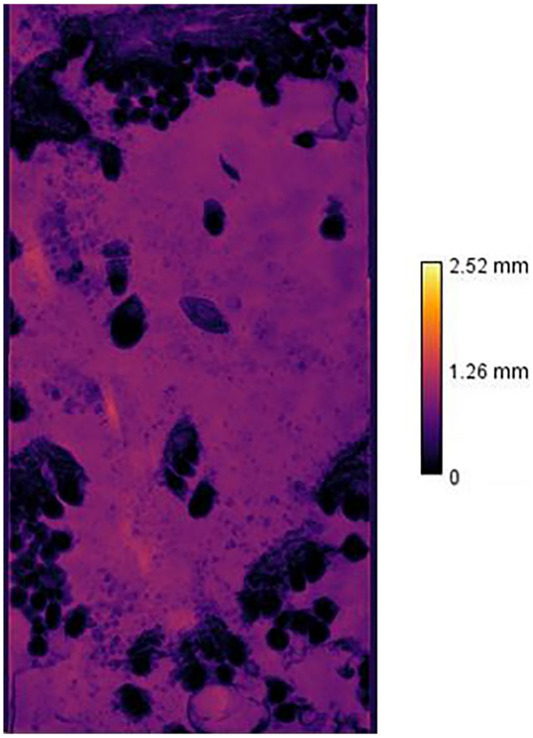

Fig. 9 Post-MICP fracture aperture map. $CaCO_3$ precipitation can be seen on surfaces inside the fracture, but the most buildup is around proppant and at the effluent side

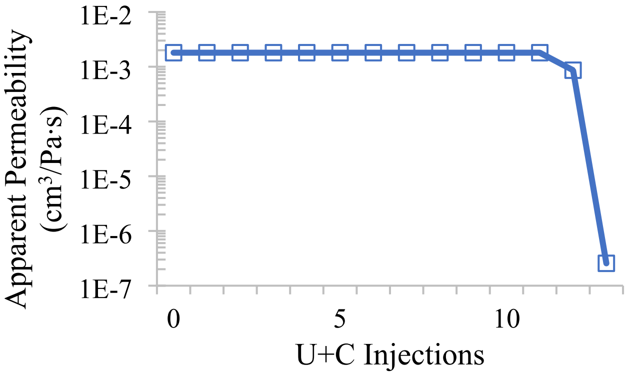

Fig. 10 Changes in apparent permeability over the course of MICP-treatment

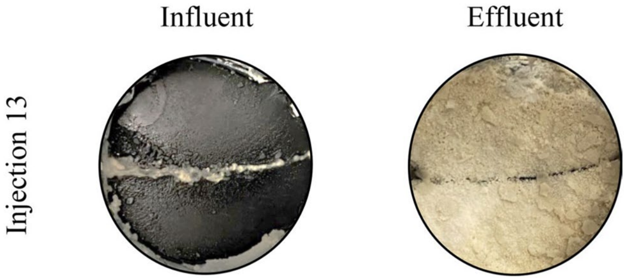

Fig. 11 Photographs of influent/effluent sides of the core without proppant after the last round of MICP-treatment

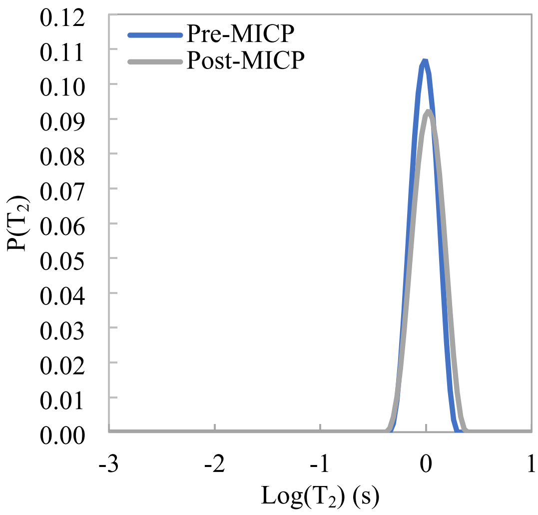

Fig. 12 Normalized T_2 distributions of a fractured, saturated Marcellus (Yawkey) shale core without proppant before (blue) and after (grey) MICP-treatment by the pulsed-flow, flow-through method. The small increase in the bulk relaxation time suggests some precipitation on surfaces inside the fracture, though the small drop in the NMR signal indicates little mineral filled the fracture space

3.4.2 Non-Invasive Analysis

Pre-MICP, the normalized T_2 profile revealed a single peak with a mode of 989 ms, indicating that the entire fracture water population behaved like 'free' water (Fig. 12). This demonstrates that proppant was likely responsible for creating multiple fracture water populations previously observed (Fig. 6). It is also noteworthy that the T_2 time of the 'free' water is 58% longer than the corresponding population in the core with proppant (Table 3). This implies a weaker surface relaxivity effect in this specific sample. Despite being extracted from the same well, shale samples can possess diverse mineralogical compositions, leading to varied responses in NMR experiments.

Post-MICP data was collected after achieving four orders of magnitude apparent permeability reduction. The marginal increase (+7.9%) in the T_2 relaxation time indicates a surface relaxivity effect due to precipitation on shale surfaces. However, the accumulated signal dropped just 6.2%, indicating little mineral formed inside the fracture. These findings are corroborated by post-MICP micro-CT analysis (Fig. 13) (preliminary micro-CT data was not collected). While dark spots appear throughout the fracture aperture map, showing

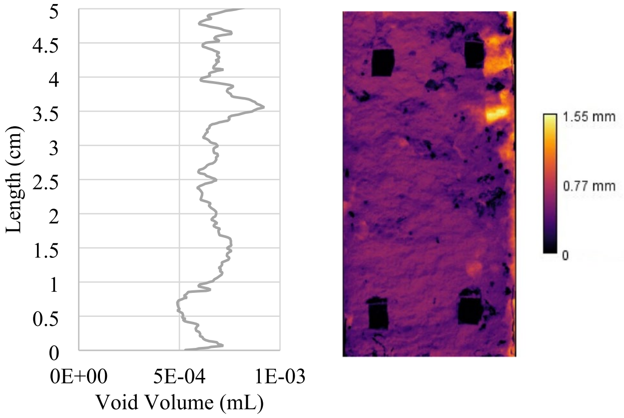

Fig. 13 Void volume calculated by micro-CT along the length of the fracture post-MICP-treatment (LHS) and the corresponding fracture aperture map (RHS). Teflon spacers (0.5 mm thick) are visible along the corners of the fracture, which kept the fracture open during flow-through treatment. There is less biomineralization within the fracture compared to the fracture sealed with proppant (Fig. 9)

small regions where mineral bridged the fracture, there are fewer signs of extensive mineralization compared to the MICP-treated fracture with proppant (Fig. 9). The results are consistent with the general observation that flow-through MICP tends to preferentially seal closer to the inlet. Indeed, at a temperature of 60 °C, which accelerates the rate of ureolysis, this effect may have been amplified, a phenomenon that has been predicted before by numerical models (Hommel et al. 2020). The flow-through studies demonstrate that distribution of proppant in the fracture and elevated temperatures may play an influential role in the extent of biomineralization achievable in shale fractures. In fractures without proppant, optimized injection strategies or agents which help improve bacterial transport may help achieve more extensive biomineralization.

3.5 Comparing Quantifiable micro-CT and NMR Results

The results so far have highlighted qualitative NMR information, with changes in T_2 relaxation times reflecting regions of mineral buildup and the extent of precipitation on surfaces inside fractures. However, NMR is inherently a quantitative tool, since the response of the NMR signal is proportional to the number of water protons inside the sample. This allows NMR to directly calculate the fracture pore volume, by taking the integrated area of the "fracture water" region of the T_2 distribution curve and comparing it to the NMR signal from a known calibration volume of saturation fluid. In contrast, micro-CT measures pore volumes more indirectly by measuring regions that lack micro-CT signal, *i.e.* everything except shale, proppant and biomineral.

While uncertainty in micro-CT measurements is introduced by the thresholding process (Sect. 2.4), uncertainty in NMR measurements depends on the signal-to-noise (S/N) ratio of the acquired NMR voltage signal (Malz and Jancke 2005; Parker and Song 2005). Pore volumes are derived from the T_2 profile, which is determined by inverse Laplace transform of the CPMG decay, an ill-posed problem (Callaghan 2011). As is standard practice, NMR S/N is increased by averaging the experiment repeatedly (see "number of scans" parameter in Table 1). Since the measured S/N of the NMR data presented in this study was on average > 100, an uncertainty of order < 1% can be inferred.

Measuring the fracture pore volume allows the amount of biomineral formed following MICP-treatment to be calculated. The total volume of calcium carbonate biomineral, $V_{CaCO_3}^{total}$, is composed of its solid and void volume fractions ($V_{CaCO_3}^{solid}$ and $V_{CaCO_3}^{void}$, respectively) (Eq. 9):

$$V_{CaCO_3}^{total} = V_{CaCO_3}^{solid} + V_{CaCO_3}^{void} \tag{9}$$

The initial void volume of the fracture, $V_{pre-MICP}^{void}$, is derived from the saturated, pre-MICP core sample measurement and consists of the difference between the total fracture volume (V_f) and the proppant volume (V_p)(Eq. 10):

$$V_{pre-MICP}^{void} = V_f - V_p \tag{10}$$

The void volume of the fracture post-MICP, $V_{post-MICP}^{void}$, is derived from the saturated, biomineralized core sample measurement and is equal to the difference between the total fracture volume and the volume of solids, which now consist of both proppant and precipitated $CaCO_3$ (Eq. 11):

$$V_{post-MICP}^{void} = V_f - V_p - V_{CaCO_3}^{solid} \tag{11}$$

The solid biomineral volume, $V_{CaCO_3}^{solid}$, is the difference between the water (void) volumes of the fracture, pre- and post-MICP (Eq. 12):

$$V_{CaCO_3}^{solid} = V_{pre-MICP}^{void} - V_{post-MICP}^{void} \tag{12}$$

Complete sets of micro-CT and NMR data were collected for the flow-through MICP-treated core with proppant (Table 4). From NMR, the initial and final void volumes were calculated to be 1.78 and 1.15 mL, respectively, resulting in 0.63 mL of solid biomineral generated after 26 rounds of MICP-treatment. From micro-CT, the initial and final void volumes were measured to be 1.71 ± 0.05 and 1.15 ± 0.08 mL, respectively, resulting in 0.6 ± 0.1 mL of $CaCO_3$ formed. In the flow-through MICP-treated core without proppant, complete sets of NMR data were collected, while only post-MICP micro-CT data was obtained. The initial volume was calculated to be 0.71 mL, which dropped to 0.67 mL post-MICP, resulting in 0.044 mL of biomineral being formed. The NMR post-MICP pore volume closely aligns to the micro-CT measurement of 0.62 ± 0.07 mL, further demonstrating the agreement between both non-invasive tools in measuring bulk properties. Note that the micro-CT pore volumes are generally slightly smaller than the NMR volumes, which may have resulted from some NaCl precipitation after drying the sample post-NMR analysis.

3.6 NMR Analysis of Immersion Biomineralized Core with Proppant

Compared to the flow-through treated Marcellus shale core with proppant (Sect. 3.3.2), the immersion treated Eagle Ford shale core displayed different T_2 distribution profiles, even before biomineralization began. Pre-MICP, the 'free' water peak dominates, and while moderate relaxation times are present, they represent a much smaller fraction of the signal compared to the flow-through core (Fig. 14). The profile suggests that proppant was evenly distributed during the NMR measurement, thereby contributing to more "clean", spread-out peaks. Additionally, the T_2 time of the 'free' water is the longest of the three fractures analyzed in this study (1.06 s), which is consistent with mineralogical differences between the shale samples (Table 2). Clay-rich Marcellus shale contains paramagnetic species that increase the surface relaxivity, whereas carbonates and quartz in Eagle Ford shale contain diamagnetic minerals that have the opposite effect (Cheng et al. 2023; Livo et al. 2020).

As with the flow-through treated core, the overall NMR signal in the immersion core dropped by approximately one-third post-MICP (-27% versus -35%, respectively) (Fig. 14). However, the 'free' water exhibited contrasting changes, moving to a shorter relaxation time (-54%) and reducing in signal intensity (-21%). While this could suggest that the applied "slug" of cells, calcium mineralizing media (CMM), and guar filled a significant portion of the void spaces inside the fracture, this is not reflected in the micro-CT data, which shows sealing mainly along the edges of the fracture (Fig. 15). This unique pattern of precipitation may reflect the method of biomineralization, in which urea and calcium are transported by diffusion inside the fracture, instead of advection as in the flow-through approach. Initial precipitation along the fracture boundaries may introduce strong mass transfer limitations of reactants inside the fracture, resulting in less sealing in this region.

Table 4 Calculating volume of solid biomineral using NMR and micro-CT. An uncertainty of order < 1% can be inferred from the NMR data

Volume (mL)	Flow-through MICP with proppant		Flow-through MICP without proppant	
	NMR	CT	NMR	CT
$V^{void}_{pre-MICP}$	1.78	1.71 ± 0.05	0.71	N/A
$V^{void}_{post-MICP}$	1.15	1.15 ± 0.08	0.67	0.62 ± 0.07
$V^{solid}_{CaCO_3}$	0.63	0.6 ± 0.1	0.044	N/A

To better understand the NMR data, a follow-up study was conducted which showed that adding brine to dried guar resulted in a similar drop in the bulk relaxation time (1.2 to 0.69 s, or -43% change). As guar polymers rehydrate, they slow the rotational tumbling of water protons, which also undergo chemical exchange with guar hydroxyl protons, leading to lower relaxation times (Hills 1992). Since a part of the seal consists of guar, this finding exposes a potential downside to this method of MICP-treatment. Past studies which combined guar and MICP indicate that the polymer played a significant role in enhancing the compressive strength of the consolidated porous media (Dikshit et al. 2021, 2022). Destructive mechanical strength testing is needed to clarify the contribution of fracture sealing from $CaCO_3$ cementation versus guar in this specific method (Bedey et al. 2023).

Because guar also contributes to the overall NMR signal, it is difficult to quantitatively determine the post-MICP volume. However, the difference between the pre-MICP NMR and post-MICP micro-CT volume measurements resulted in

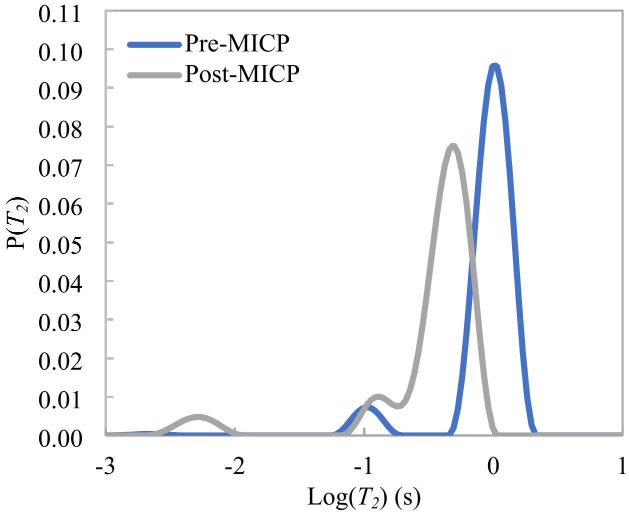

Fig. 14 Normalized T_2 distributions of a fractured, saturated Eagle Ford shale core with proppant before (blue) and after (grey) MICP-treatment by the immersion method. The shift of the 'free' water population to a shorter relaxation time implies a large void volume change inside the fracture, which is not reflected in the micro-CT data. This discrepancy can be attributed to the presence of guar enhancing T_2 relaxation

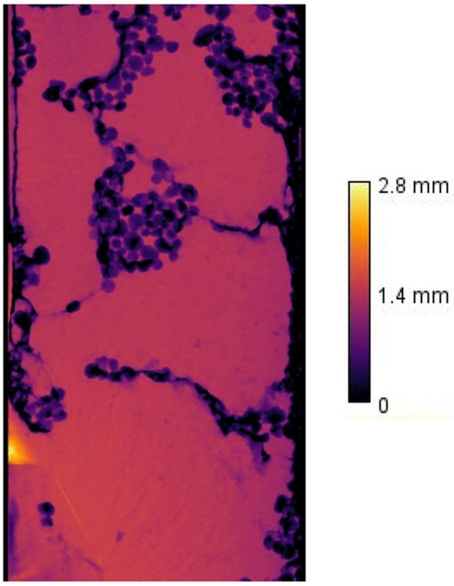

Fig. 15 Post-MICP fracture aperture map. Sealing has occurred primarily along the edges, with large void volumes visible throughout the fracture

0.41 ± 0.06 mL of the fracture filled, or 22% of the initial volume (Table 5) (preliminary micro-CT data was not collected). This represents a smaller change compared to the flow-through approach, which is unsurprising since a single application of MICP via the immersion method is unlikely to fill the fracture as thoroughly as multiple pulsed-flow injections of cells and urea and calcium (U + C). Overall, while the single-shot, polymer-based MICP-treatment strategy has potential to be much more efficient than traditional, water-based MICP-treatment, it does not appear any less susceptible to inhomogeneous sealing and methods for delivery still need to be established.

Table 5 Void volume measurements of core treated with immersion MICP-treatment

Volume (mL)	Immersion MICP-treatment
$V^{void}_{pre-MICP}$	1.84
$V^{void}_{post-MICP}$	1.43 ± 0.06
ΔV	0.41 ± 0.06

Pre- and Post-MICP volumes were calculated with NMR and micro-CT, respectively

4 Conclusions

Non-invasive NMR tools can be used to study MICP-treatment of shale fractures. T_1-T_2 correlations identified distinct hydrogen populations attributed to shale organics, shale pore water, and fracture water. Rapid T_2 experiments were used to determine the degree of fracture sealing by providing details about regions associated with mineral buildup and extent of precipitation on surfaces. NMR also provided quantitative information, with pore volume measurements demonstrating agreement with micro-CT measurements.

After 26 injections of pulsed-flow, flow-through MICP-treatment of a shale fracture at 60°C, the apparent permeability was reduced by approximately four orders of magnitude, though proppant was found to influence the distribution of precipitation. Without proppant, the inlet side of the core sealed after 13 injections and before filling most of the fracture. Comparatively, the single-shot, polymer-based “immersion” MICP-treatment method sealed the shale fracture more efficiently at 60°C. However, micro-CT images revealed that sealing was limited to the edges of the fracture and trends in the T_2 profile suggest that guar in the seal rehydrated when saturated.

Overall, both NMR and micro-CT are valuable for studying MICP fracture sealing strategies. Micro-CT offers highly detailed spatial information, but only low-field NMR relaxometry has the potential to monitor future subsurface biomineralization progress (Kirkland et al. 2017; Kirkland and Codd 2018). The findings of this study can guide the application of NMR logging tools in tracking subsurface remediation efforts.

Appendix A (Fig. 16)

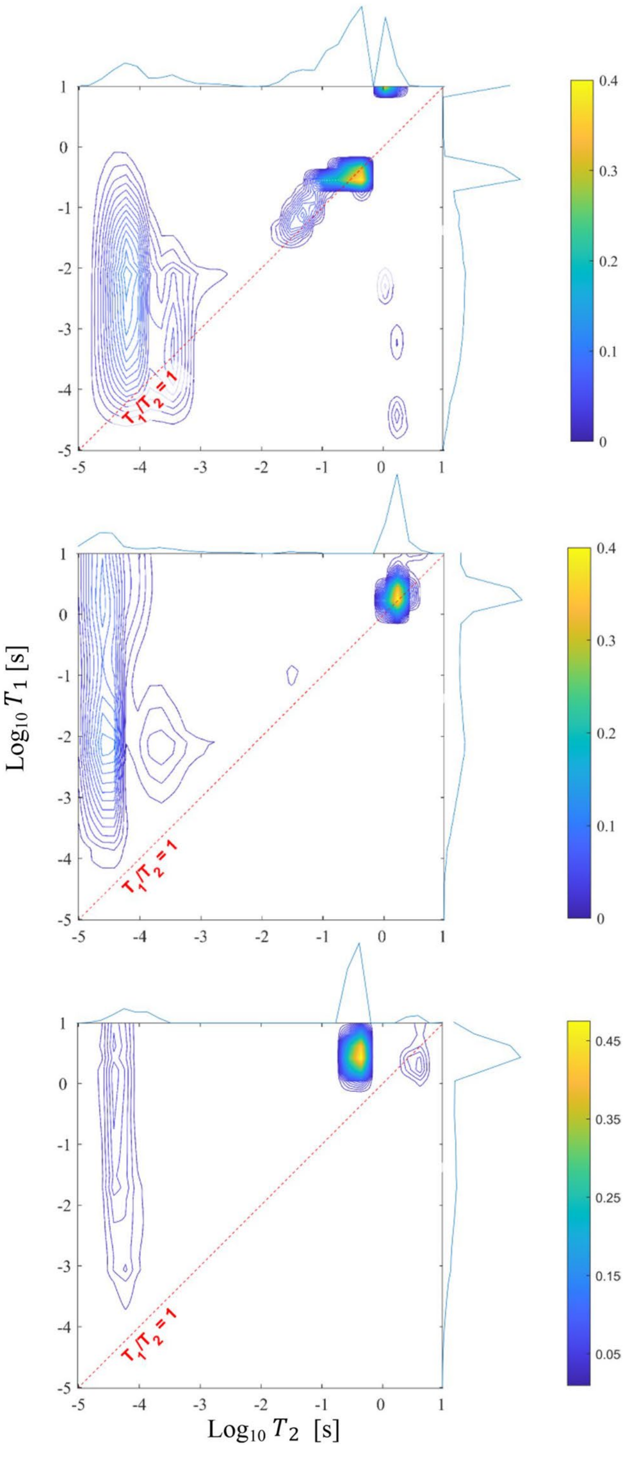

Fig. 16 T_1-T_2 maps of satruated, fractured shale samples pre-MICP-treatment. From top to bottom: Marcellus (Yawkey) shale with proppant treated with flow-through MICP, Marcellus (Yawkey) shale without proppant treated with flow-through MICP, and Eagle Ford shale with proppant treated with immersion MICP. Experiments demonstrate that "fracture water" populations are distinct from other shale hydrogen populations

Appendix B (Table 6)

Table 6 Flowrates, pressures, and apparent permeability per injection for each core sealed using flow-through MICP

Injection	Core with Proppant			Core without Proppant		
	Q (mL/min)	ΔP (psi)	Apparent permeability (cm^3/Pa•s)	Q (mL/min)	ΔP (psi)	Apparent permeability (cm^3/Pa•s)
1	5	0.708	1.7×10^{-3}	5	0.67	1.8×10^{-3}
2	5	0.708	1.7×10^{-3}	5	0.67	1.8×10^{-3}
3	5	0.708	1.7×10^{-3}	5	0.67	1.8×10^{-3}
4	5	0.708	1.7×10^{-3}	5	0.67	1.8×10^{-3}
5	5	0.708	1.7×10^{-3}	5	0.67	1.8×10^{-3}
6	5	0.708	1.7×10^{-3}	5	0.67	1.8×10^{-3}
7	5	0.708	1.7×10^{-3}	5	0.67	1.8×10^{-3}
8	5	0.708	1.7×10^{-3}	5	0.67	1.8×10^{-3}
9	5	0.708	1.7×10^{-3}	5	0.67	1.8×10^{-3}
10	5	0.708	1.7×10^{-3}	5	0.67	1.8×10^{-3}
11	5	0.708	1.7×10^{-3}	5	0.67	1.8×10^{-3}
12	5	0.708	1.7×10^{-3}	5	0.67	1.8×10^{-3}
13	5	0.708	1.7×10^{-3}	5	1.4	8.6×10^{-4}
14*	5	0.708	1.7×10^{-3}	0.025	23.6	2.6×10^{-7}
15	5	0.708	1.7×10^{-3}	N/A	N/A	N/A
16	5	0.708	1.7×10^{-3}	N/A	N/A	N/A
17	5	0.708	1.7×10^{-3}	N/A	N/A	N/A
18	1	1.1	2.2×10^{-4}	N/A	N/A	N/A
19	1	1.6	1.5×10^{-4}	N/A	N/A	N/A
20	1	6	4.0×10^{-5}	N/A	N/A	N/A
21	0.25	26.5	2.3×10^{-6}	N/A	N/A	N/A
22	0.1	24.9	9.7×10^{-7}	N/A	N/A	N/A
23	0.1	25.8	9.4×10^{-7}	N/A	N/A	N/A
24	0.1	23.2	1.0×10^{-6}	N/A	N/A	N/A
25	0.125	25.2	1.2×10^{-6}	N/A	N/A	N/A
26	0.2	27.9	1.7×10^{-6}	N/A	N/A	N/A
27**	0.03	22	3.3×10^{-7}	N/A	N/A	N/A

*For core without proppant, “injection 14” was a permeability test, not another round of MICP-treatment

**For core with proppant, “injection 27” was a permeability test, not another round of MICP-treatment

Acknowledgements The authors express their gratitude to Dr. Evan McCarney, Korimako Chemical Limited, for establishing the RCA at the MSU Magnetic Resonance Lab. This research benefited from ICAL facilities at MSU, which is supported by the National Science Foundation (Grant No. ECCS-2025391). The authors acknowledge Sub-Zero Science and Engineering Research facility at MSU for use of the X-Ray micro-CT scanner and data processing and analysis software. Special appreciation is also reserved for Magdalena Gill, NETL, for her expertise in processing micro-CT data in Fiji. Additional funding for the LBNL author was provided by the U.S. Department of Energy under contract No. DE-AC0205CH11231 to the Lawrence Berkeley National Laboratory. This study was supported by funding from the US Department of Energy, Office of Basic Earth Sciences, DOE Award No.: DE-SC0021324. Any opinions, findings, conclusions, or recommendations expressed herein are those of the authors and do not necessarily reflect the views of the Department of Energy (DOE).

Author Contributions CMK and AJP conceived and directed the research, obtained grant funding, and contributed to the experimental design. MRW and KB contributed to the experimental design, material preparation, and data collection. MRW conducted NMR experiments and data analysis with guidance from CMK and JDS. KB and DC conducted micro-CT experiments, and data analysis was performed by KB and MRW, with guidance from DC. MRW created figures and wrote the manuscript, with input from all authors during the revision and rewriting process.

Funding US Department of Energy, DE-SC0021324, Catherine M. Kirkland.

Data Availability The datasets generated and analyzed during the current study are available from the corresponding author on reasonable request.

Declarations

Conflict of Interest All authors declare they have no known conflict of interest.

References

Anjum S (2023) Material properties of ureolytically induced calcium carbonate composites [Doctor of Philosophy, Montana State University].

Bachmeier KL, Williams AE, Warmington JR, Bang SS (2002) Urease activity in microbiologically-induced calcite precipitation. J Biotechnol 93(2):171–181. https://doi.org/10.1016/S0168-1656(01)00393-5

Barba R, Allison J, Villarreal M (2022) A Comparison of Latest Generation Frac New Well and Refrac Results with Evidence of Refrac Reorientation. 10th Unconventional Resources Technology Conference, Houston, Texas. https://doi.org/10.15530/urtec-2022-3724057

Bedey K, Willett MR, Cunningham AB, Phillips AB, Kirkland CM, Dobeck L, Eldring J, Crandall D, Rutqvist J (2023) Developing Methods to Assess Changes in Mechanical Properties of Shale Modified by Engineered Mineral Precipitation. 57th U.S. Rock Mechanics/Geomechanics Symposium, Atlanta, GA. https://doi.org/10.56952/ARMA-2023-0807

Blümich B (2005) Essential NMR for scientists and engineers. Springer

Brownstein KR, Tarr CE (1979) Importance of classical diffusion in NMR studies of water in biological cells. Phys Rev 19(6):2446–2453. https://doi.org/10.1103/PhysRevA.19.2446

Callaghan PT (1991) Principles of nuclear magnetic resonance microscopy. Oxford University Press, Oxford

Callaghan PT (2011) Translational dynamics and magnetic resonance: principles of pulsed gradient spin echo NMR. Oxford University Press, Oxford

Callaghan PT, Godefroy S, Ryland BN (2003) Diffusion–relaxation correlation in simple pore structures. J Magn Reson 162(2):320–327. https://doi.org/10.1016/S1090-7807(03)00056-9

Cheng J, Xia X, Wang L (2023) Determining nuclear magnetic resonance surface relaxivity of shales. Energy Fuels 37(7):4986–4995. https://doi.org/10.1021/acs.energyfuels.2c04116

Cladouhos TT, Petty S, Swyer MW, Uddenberg ME, Grasso K, Nordin Y (2016) Results from Newberry Volcano EGS demonstration, 2010-2014. Geothermics 63(C):44–61. https://doi.org/10.1016/j.geothermics.2015.08.009

Crandall D, Mackey P, Paronish T, Brown S, Moore J, Workman S, Warden L (2019) Computed Tomography Scanning and Geophysical Measurements of the Rhinestreet and Marcellus Shale from the Yawkey #98 Well U.S. Department of Energy, National Energy Technology Laboratory. https://doi.org/10.18141/1502092

Cunningham AB, Gerlach R, Phillips A, Lauchnor E, Rothman R, Hiebert R, Busch A, Lomans BP, Sprangler L (2015) Assessing Potential for Biomineralization Sealing in Fractured Shale at the Mont Terri Underground Research Facility, Switzerland. In Carbon Dioxide Capture for Storage in Deep Geological Formations Vol. 4. CPL Press and BP. pp. 887–903.

Cuthbert MO, McMillan LA, Handley-Sidhu S, Riley MS, Tobler DJ, Phoenix VR (2013) A field and modeling study of fractured rock permeability reduction using microbially induced calcite precipitation. Environ Sci Technol 47(23):13637–13643. https://doi.org/10.1021/es402601g

De Muynck W, De Belie N, Verstraete W (2010) Microbial carbonate precipitation in construction materials: a review. Ecol Eng 36(2):118–136. https://doi.org/10.1016/j.ecoleng.2009.02.006

Dikshit R, Dey A, Gupta N, Varma SC, Venugopal I, Viswanathan K, Kumar A (2021) Space bricks: from LSS to machinable structures via MICP. Ceram Int 47(10):14892–14898. https://doi.org/10.1016/j.ceramint.2020.07.309

Dikshit R, Gupta N, Dey A, Viswanathan K, Kumar A (2022) Microbial induced calcite precipitation can consolidate martian and lunar regolith simulants. PLoS ONE 17(4):e0266415. https://doi.org/10.1371/journal.pone.0266415

Espinoza DN, Santamarina JC (2017) CO_2 breakthrough—caprock sealing efficiency and integrity for carbon geological storage. Int J Greenhouse Gas Control. 66:218–229. https://doi.org/10.1016/j.ijggc.2017.09.019

Fleury M, Romero-Sarmiento M (2016) Characterization of shales using T1–T2 NMR maps. J Petrol Sci Eng 137:55–62. https://doi.org/10.1016/j.petrol.2015.11.006

Golsanami N, Sun J, Zhang Z (2016) A review on the applications of the nuclear magnetic resonance (NMR) technology for investigating fractures. J Appl Geophys 133:30–38. https://doi.org/10.1016/j.jappgeo.2016.07.026

Gupta A, Stait-Gardner T, Price WS (2021) Is it time to forgo the use of the terms "spin-lattice" and "spin-spin" relaxation in NMR and MRI? J Phys Chem Lett 12(27):6305–6312. https://doi.org/10.1021/acs.jpclett.1c00945

Hansen FD, Hardin EL, Rechard RP, Freeze GA, Sassani DC, Brady PV, Stone CM, Martinez MJ, Holland JF, Dewers T, Gaither KN, Sobolik SR, Cygan RT (2010) Shale Disposal of U.S. High-Level Radioactive Waste. Sandia National Laboratories, Albuquerque, New Mexico.

Hasan MR, Reza MT (2019) Hydrothermal deformation of Marcellus shale: effects of subcritical water temperature and holding time on shale porosity and surface morphology. J Petrol Sci Eng 172:383–390. https://doi.org/10.1016/j.petrol.2018.09.078

Hills BP (1992) The proton exchange cross-relaxation model of water relaxation in biopolymer systems. Mol Phys 76(3):509–523. https://doi.org/10.1080/00268979200101501

Hommel J, Akyel A, Frieling Z, Phillips AJ, Gerlach R, Cunningham AB, Class H (2020) A numerical model for enzymatically induced calcium carbonate precipitation. Appl Sci 10(13):4538. https://doi.org/10.3390/app10134538

Jain S, Fang C, Achal V (2021) A critical review on microbial carbonate precipitation via denitrification process in building materials. Bioengineered 12(1):7529–7551. https://doi.org/10.1080/21655979.2021.1979862

Jeanne P, Zhang Y, Rutqvist J (2020) Influence of hysteretic stress path behavior on seal integrity during gas storage operation in a depleted reservoir. J Rock Mech Geotech Eng. 12(4):886–899. https://doi.org/10.1016/j.jrmge.2020.06.002

Jin G, Xu K, Xu C, Huang M, Qasem A, Ghaleb R, Guo S, Liu S (2020) Cementation of shale soils by MICP technology and its damage characteristics due to freeze-thaw weathering processes. J Cold Reg Eng. https://doi.org/10.1061/(asce)cr.1943-5495.0000229

Jung H (2021) Basic physical principles and clinical applications of computed tomography. Progr Med Phys 32(1):1–17. https://doi.org/10.14316/pmp.2021.32.1.1

Kim G, Kim J, Youn H (2018) Effect of temperature, pH, and reaction duration on microbially induced calcite precipitation. Appl Sci. https://doi.org/10.3390/app8081277

Kirkland CM, Codd SL (2018) Low-field borehole NMR applications in the near-surface environment. Vadose Zone Journal 17(1):1–11. https://doi.org/10.2136/vzj2017.01.0007

Kirkland CM, Zanetti S, Grunewald E, Walsh DO, Codd SL, Phillips AJ (2017) Detecting microbially induced calcite precipitation in a model well-bore using downhole low-field NMR. Environ Sci Technol 51(3):1537–1543. https://doi.org/10.1021/acs.est.6b04833

Kirkland CM, Norton D, Firth O, Eldring J, Cunningham AB, Gerlach R, Phillips AJ (2019) Visualizing MICP with X-ray μ-CT to enhance cement defect sealing. Int J Greenhouse Gas Control 86:93–100. https://doi.org/10.1016/j.ijggc.2019.04.019

Kirkland CM, Thane A, Hiebert R, Hyatt R, Kirksey J, Cunningham AB, Gerlach R, Spangler L, Phillips AJ (2020) Addressing wellbore integrity and thief zone permeability using microbially-induced calcium carbonate precipitation (MICP): a field demonstration. J Petrol Sci Eng. https://doi.org/10.1016/j.petrol.2020.107060

Kirkland CM, Akyel A, Hiebert R, McCloskey J (2021) Ureolysis-induced calcium carbonate precipitation (UICP) in the presence of CO_2-affected brine: a field demonstration. Int J Greenhouse Gas Control. https://doi.org/10.1016/j.ijggc.2021.103391

Kleinberg RL, Kenyon WE, Mitra PP (1994) Mechanism of NMR relaxation of fluids in rock. J Magn Reson, Ser A 108(2):206–214. https://doi.org/10.1006/jmra.1994.1112

Livo K, Saidian M, Prasad M (2020) Effect of paramagnetic mineral content and distribution on nuclear magnetic resonance surface relaxivity in organic-rich Niobrara and Haynesville shales. Fuel (guildford) 269:117417. https://doi.org/10.1016/j.fuel.2020.117417

Malz F, Jancke H (2005) Validation of quantitative NMR. J Pharm Biomed Analysis 38(5):813–823. https://doi.org/10.1016/j.jpba.2005.01.043

Meng Y, Zhao F, Jin X, Feng Y, Sun G, Lin J, Jia B, Li P (2021) Performance evaluation of enzyme breaker for fracturing applications under simulated reservoir conditions. Molecules. https://doi.org/10.3390/molecules26113133

Minto JM, Hingerl FF, Benson SM, Lunn RJ (2017) X-ray CT and multiphase flow characterization of a 'bio-grouted' sandstone core: the effect of dissolution on seal longevity. Int J Greenhouse Gas Control 64:152–162. https://doi.org/10.1016/j.ijggc.2017.07.007

Mukhametdinova A, Habina-Skrzyniarz I, Kazak A, Krzyżak A (2021) NMR relaxometry interpretation of source rock liquid saturation—a holistic approach. Marine Petrol Geol. https://doi.org/10.1016/j.marpetgeo.2021.105165

Parker RL, Song YQ (2005) Assigning uncertainties in the inversion of NMR relaxation data. J Magn Reson 174(2):314–324. https://doi.org/10.1016/j.jmr.2005.03.002

Petty S, Nordin Y, Glassely W, Cladouhos T (2013) Improving geothermal project economics with multi-zone stimulation: results from the Newberry Volcano EGS Demonstration. 38th Workshop on Geothermal Reservoir Engineering, Stanford, CA.

Phillips AJ, Gerlach R, Lauchnor E, Mitchell AC, Cunningham AB, Spangler L (2013) Engineered applications of ureolytic biomineralization: a review. Biofouling 29(6):715–733. https://doi.org/10.1080/08927014.2013.796550

Phillips AJ, Cunningham AB, Gerlach R, Hiebert R, Hwang C, Lomans BP, Westrich J, Mantilla C, Kirksey J, Esposito R, Spangler L (2016) Fracture sealing with microbially-induced calcium carbonate precipitation: a field study. Environ Sci Technol 50(7):4111–4117. https://doi.org/10.1021/acs.est.5b05559

Phillips AJ, Troyer E, Hiebert R, Kirkland C, Gerlach R, Cunningham AB, Spangler L, Kirksey J, Rowe W, Esposito R (2018) Enhancing wellbore cement integrity with microbially induced calcite precipitation (MICP): a field scale demonstration. J Petrol Sci Eng 171:1141–1148. https://doi.org/10.1016/j.petrol.2018.08.012

Rutqvist J (2012) The geomechanics of CO_2 storage in deep sedimentary formations. Geotech Geol Eng 30(3):525–551. https://doi.org/10.1007/s10706-011-9491-0

Sang G, Lunn RJ, Minto JM, El Mountassir G (2022) microbially induced calcite precipitation for sealing anhydrite fractures with gouges 56th US Rock Mechanics/Geomechanics Symposium, Santa Fe, New Mexico. https://doi.org/10.56952/ARMA-2022-0277

Schindelin J, Arganda-Carreras I, Frise E, Kaynig V, Longair M, Pietzsch T, Preibisch S, Rueden C, Saalfeld S, Schmid B, Tinevez J-Y, White DJ, Hartenstein V, Eliceiri K, Tomancak P, Cardona A (2012) Fiji: an open-source platform for biological-image analysis. Nat Methods 9(7):676–682. https://doi.org/10.1038/nmeth.2019

Sham E, Mantle MD, Mitchell J, Tobler DJ, Phoenix VR, Johns ML (2013) Monitoring bacterially induced calcite precipitation in porous media using magnetic resonance imaging and flow measurements. J Contam Hydrol 152:35–43. https://doi.org/10.1016/j.jconhyd.2013.06.003

Soeder DJ (2018) The successful development of gas and oil resources from shales in North America. J Pet Sci Eng 163:399–420. https://doi.org/10.1016/j.petrol.2017.12.084

Thrane LW, Daily RL, Thane A, Kirkland CM, McCarney ER, Dykstra R, Codd SL, Phillips AJ (2020) Detecting microbially induced calcium carbonate precipitation in porous systems using low-field nuclear magnetic resonance relaxometry. J Geotech Geoenviron Eng. https://doi.org/10.1061/(asce)gt.1943-5606.0002226

Tobler DJ, Minto JM, El Mountassir G, Lunn RJ, Phoenix VR (2018) Microscale Analysis of Fractured Rock Sealed With Microbially Induced $CaCO_3$ Precipitation: Influence on Hydraulic and Mechanical Performance. Water Resour Res 54(10):8295–8308. https://doi.org/10.1029/2018wr023032

Turner R, Castro GM, Minto J, El Mountassir G, Lunn RJ (2023) Treatment of fractured concrete via microbially induced carbonate precipitation: From micro-scale characteristics to macro-scale behaviour. Constr Buil Mater. https://doi.org/10.1016/j.conbuildmat.2023.131467

Venkataramanan L, Yi-Qiao S, Hurlimann MD (2002) Solving Fredholm integrals of the first kind with tensor product structure in 2 and 2.5 dimensions. IEEE Trans Signal Process. 50(5):1017–1026. https://doi.org/10.1109/78.995059

Wang X, Tao J (2018) Polymer-modified microbially induced carbonate precipitation for one-shot targeted and localized soil improvement. Acta Geotech 14(3):657–671. https://doi.org/10.1007/s11440-018-0757-z

Wang Y, Wang Y, Soga K, DeJong JT, Kabla AJ (2023) Microscale investigations of temperature-dependent microbially induced carbonate precipitation (MICP) in the temperature range 4–50 °C. Acta Geotech 18(4):2239–2261. https://doi.org/10.1007/s11440-022-01664-9

Wang Y (2018) Microbial-Induced Calcium Carbonate Precipitation: from Micro to Macro Scale [Doctor of Philosophy, University of Cambridge].

Washburn KE (2014) Relaxation mechanisms and shales. Concepts in Magnetic Resonance Part A 43A(3):57–78. https://doi.org/10.1002/cmr.a.21302

Whiffin VS (2004). Microbial $CaCO_3$ Precipitation for the production of Biocement [Doctor of Philosophy, Murdoch University]. Perth, Australia.

Wu J, Wang X-B, Wang H-F, Zeng RJ (2017) Microbially induced calcium carbonate precipitation driven by ureolysis to enhance oil recovery. RSC Adv 7(59):37382–37391. https://doi.org/10.1039/c7ra05748b

Zamiri MS, MacMillan B, Marica F, Guo J, Romero-Zerón L, Balcom BJ (2021) Petrophysical and geochemical evaluation of shales using magnetic resonance T_1–T_{2*} relaxation correlation. Fuel. https://doi.org/10.1016/j.fuel.2020.119014

Zamiri MS, Marica F, Romero-Zerón L, Balcom BJ (2022) Monitoring shale water uptake using 2D magnetic resonance relaxation correlation and SPRITE MRI. Chem Eng J 428:131042. https://doi.org/10.1016/j.cej.2021.131042

Zhang P, Lu S, Li J, Chang X (2020) 1D and 2D nuclear magnetic resonance (NMR) relaxation behaviors of protons in clay, kerogen and oil-bearing shale rocks. Marine Petrol Geol. https://doi.org/10.1016/j.marpetgeo.2019.104210

Zhuang C, Liu C, Cui Z, Yang Z, Chen Y, Dou Z (2022) Microbially-induced calcium carbonate precipitation test on yellow sandstone based on LF-NMR monitoring. Int J Environ Res Public Health. https://doi.org/10.3390/ijerph192416860

Zimmerman RW, Bodvarsson GS (1996) Hydraulic conductivity of rock fractures. Transp Porous Media 23(1):1–30. https://doi.org/10.1007/BF00145263

Zivar D, Kumar S, Foroozesh J (2021) Underground hydrogen storage: a comprehensive review. Int J Hydrogen Energy 46(45):23436–23462. https://doi.org/10.1016/j.ijhydene.2020.08.138

Authors and Affiliations

Matthew R. Willett[1,2] · **Kayla Bedey**[2,3] · **Dustin Crandall**[4] · **Joseph D. Seymour**[1,2] · **Jonny Rutqvist**[5] · **Alfred B. Cunningham**[2,3] · **Adrienne J. Phillips**[2,3] · **Catherine M. Kirkland**[2,3]

✉ Matthew R. Willett
matthewwillett@montana.edu

Kayla Bedey
kaylabedey@montana.edu

Dustin Crandall
Dustin.Crandall@NETL.DOE.GOV

Joseph D. Seymour
jseymour@montana.edu

Jonny Rutqvist
jrutqvist@lbl.gov

Alfred B. Cunningham
al_c@montana.edu

Adrienne J. Phillips
adrienne.phillips@montana.edu

Catherine M. Kirkland
catherine.kirkland@montana.edu

[1] Department of Chemical Engineering, Montana State University, Bozeman, MT, USA

[2] Center for Biofilm Engineering, Montana State University, Bozeman, MT, USA

[3] Department of Civil Engineering, Montana State University, Bozeman, MT, USA

[4] National Energy Technology Laboratory, Morgantown, WV, USA

[5] Lawrence Berkeley National Laboratory, Berkeley, CA, USA